Korean J. Chem. Eng., 36(1), 115-125 (2019)
DOI: 10.1007/s11814-018-0148-z

pISSN: 0256-1115
eISSN: 1975-7220

Enhanced photocatalytic activity of TiO_2/graphene by tailoring oxidation degrees of graphene oxide for gaseous mercury removal

Yu Guan*, Tao Hu*,, Jiang Wu*,†, Lili Zhao*,†, Fengguo Tian***,†, Weiguo Pan*, Ping He*, Xuemei Qi*, Fangqin Li*, and Kai Xu***

*College of Energy and Mechanical Engineering, Shanghai University of Electric Power, Shanghai 200090, China
**Huadian Weifang Power Generation Co., Ltd., Weifang 261000, China
***College of Environmental Sciences and Engineering, Donghua University, Shanghai 202620, China
(*Received 7 April 2018 • accepted 3 September 2018*)

Abstract−We used a simple method of graphene oxide (GO) preparation with different oxidation levels, and control the properties of the TiO_2 nanocrystals by tuning the content and oxidation degree of GO to enhance the photocatalytic performance. During the hydrothermal reaction, reduction of GO, formation of TiO_2 and chemical bonds between TiO_2 and reduced graphene oxide (RGO) was achieved simultaneously. Characterization results showed that TiO_2 properties such as crystalline grain and particle size could be tailored by the amount of functional groups, and that crystallinity was also controlled by GO degrees of oxidation. TiO_2/RGO photocatalysts showed great efficiency of mercury oxidation, which reached 83.7% and 43.6% under UV and LED light irradiation, respectively. The effects of crystalline grain size and surface chemical properties on Hg^0 removal under LED and UV light irradiation were analyzed. In addition, the properties of the photocatalysts before and after UV illumination were investigated, finding that part of Ti-OH on TiO_2 surface transformed to Ti-O-Ti. In a nutshell, this work could provide a new insight into enhancing activity of photocatalysts and understanding the photocatalytic mechanism.

Keywords: TiO_2, Reduced Graphene Oxide, Photocatalysis, Chemical Bonds, Elemental Mercury

INTRODUCTION

Mercury is a toxic and persistent trace metal, causing mortality, reproductive failure, and other health effects in predatory wildlife and humans. As a result of anthropogenic activities, mercury emissions to the environment have increased significantly [1,2]. Delegates from 128 countries met in Geneva, Switzerland and all have agreed that it is urgent to reduce mercury emissions [3]. Among various strategies of Hg^0 removal, photocatalytic oxidation of Hg^0, which has a higher oxidation ability and no secondary pollution, has attracted renewed attention among researchers [4,5].

It is widely known that TiO_2 is the most researched photocatalytic material, which has been extensively used as a standard photocatalyst because of its long-term thermodynamic stability, relatively low toxicity, excellent photocatalytic performance and low cost compared to other semiconductor materials [6-8]. However, bare TiO_2 usage still presents several limitations in practical applications: (i) photo-generated electron-hole pairs can recombine quickly, which results in a low photo-oxidation rate [9-11], and (ii) TiO_2 can only be excited under ultraviolet (UV) irradiation, which is less than 5% of the total solar radiation due to its wide band gap [12,13]. What's more, TiO_2 photocatalytic activity can be affected by many aspects, including crystal phase, crystalline grain size, surface chemical properties, specific surface area and crystallinity [14]. Besides, if the size of the TiO_2 crystalline grain is small, and this is favorable to increase the number of reactive sites to improve the performance on surface redox reactions, the photo-generated electron will be easily recombined with the hole. Meanwhile, high crystallinity can improve the catalytic activity of TiO_2 by enhancing charge separation efficiency, which is usually needed to further thermal treatment. However, thermal treatment at high temperatures may lead to larger particles, and deteriorate photocatalytic performance. Hence, it is necessary to maintain a balance between the size of the crystalline grain and degree of crystallinity [15].

Graphene, due to its excellent charge carrier mobility, large specific surface area, high transparency and good electrical conductivity [16-19], can be selected to prepare composites with TiO_2 to offer unique advantages for photocatalytic decontamination of air and water [20]. The composite TiO_2/RGO has three properties: the excellent absorptivity of pollutants, extended light absorption range into the visible region, facile charge transportation and separation to reduce electron/hole pair recombination [21,22]. Therefore, it is expected to become one of the most promising materials in the next generation of photocatalysts.

So far, there are three major methods to synthesize GO, a precursor of RGO. (i) the Brodie method [23], (ii) the Staudenmaier method [24], and (iii) the Hummers method [25]. In this work, we report a simple method to prepare different oxidation levels of GO without careful temperature control and experimental operation. As far as we know, GO could be an ideal substrate for grow-

†To whom correspondence should be addressed.
E-mail: wjcfd2002@sina.com, zhaolili@shiep.edu.cn, fg.tian@dhu.edu.cn
‡Yu Guan and Tao Hu contributed equally to this work.

ing and anchoring of functional nanocrystals for high-performance photocatalysts. The decoration of TiO_2 nanoparticles on GO sheets has been studied [26,27]. There are few references on how to control the properties of nanocrystal growth on RGO by tuning the oxidation degree of the GO. Herein, we rationalize the nanocrystal growth behavior to enhance the photocatalytic performance of TiO_2/RGO composites.

In the present work, TiO_2/RGO composites were prepared through adding different content and different oxidation degree of GO to investigate their effect on the crystalline grain size, surface chemical properties and crystallinity, in turn, on Hg^0 removal under LED and UV light irradiation, respectively. Moreover, the properties of the photocatalyst after UV irradiation were explored and the reaction mechanism was discussed based on the experimental and characterization results.

EXPERIMENTAL

1. Materials and Reagents

Flake graphite (325 mesh) was purchased from Qingdao Xingyuan graphite milk Co., Ltd. All the chemicals were supplied from Sinopharm Chemical Reagent (Shanghai, China).

2. Preparation of Graphene Oxide (GO)

GO was synthesized by pressurized oxidation [28,29]. Four 100 mL Teflon reactor was placed in a stainless steel autoclave, which was completely dried in drying oven and cooled at 0-10 °C. The flake graphite (0.5 g) and $KMnO_4$ (3 g) were put into the beaker, and a 9 : 1 mixture of concentrated H_2SO_4/H_3PO_4 (36 : 4 mL) was added and stirred at the same time. As soon as the mixture was added, the mixture was transferred from the beaker to the reactor and was fastened down. The autoclaves were kept 80 °C for 3 h, 5 h, 7 h and 9 h, respectively, and then cooled at ambient temperature, and they were named as GO(3), GO(5), GO(7) and GO(9), respectively. The obtained mud was transferred to a beaker and diluted slowly with 260 mL of water. With magnetic stirring, H_2O_2 (30%) was dripped into the suspension until the slurry turned bright yellow. The suspension was washed with HCl solution and deionized water until the pH reached 7, and GO suspension was obtained. After exfoliation by sonication of GO dispersion for 3 h, the GO was dried by vacuum freeze drier.

3. Preparation of TiO_2/RGO Composites

TiO_2/RGO composites were synthesized by $Ti(SO_4)_2$ and GO. In a typical preparation process, 0.48 g $Ti(SO_4)_2$ was added into 15 mL of ethanol and then a certain amount of GO was added into the solution. Subsequently, deionized water was added to get a total volume of 45 mL gradually. After being stirred for 30 min, the obtained solution was sonicated for 1 hour in the ultrasonic cleaning machine, and then transferred into a 50 mL Teflon-sealed autoclave maintained at 150 °C for 24 h in an oven. After being cooled at room temperature, the composites were washed with deionized water several times and then they were dried in vacuum freeze drier. The as-prepared TiO_2/RGO composites with 0.4 mg, 0.8 mg, 1.6 mg, and 3.2 mg GO(3), in the starting solution were referred to as TiO_2/RGO-1, TiO_2/RGO-2, TiO_2/RGO-3, TiO_2/RGO-4, respectively. In the same way, the as-prepared TiO_2/RGO composites with 4 mg GO(3), GO(5), GO(7) and GO(9) in the starting solution prepared by this procedure were denoted as TiO_2/RGO(3), TiO_2/RGO(5), TiO_2/RGO(7), TiO_2/RGO(9), respectively. For comparison, pure TiO_2 particles and RGO were also prepared under the same conditions in the absence of GO and $Ti(SO_4)_2$, respectively.

4. Characterization

The morphology of the samples was observed by a field emission scanning electron microscope (FE-SEM, Phillips XL-30 FEG/NEW). Transmission electron microscopy (TEM) and high-resolution transmission electron microscopy (HRTEM) image were performed to further analyze the morphology and crystallinity of the products on a Phillips Model CM200 transmission electron microscope. Nitrogen adsorption-desorption isotherms were obtained at liquid nitrogen temperature (–196 °C) using a nitrogen adsorption apparatus (ASAP 2020, USA). All the samples were degassed at 100 °C prior to measurements. The specific surface area was determined from the linear part of the Brunauer-Emmett-Teller (BET) equation (P/P_0=0.05-0.25). Cumulative pore volumes and pore diameters are calculated from the adsorption isotherms using the Barrett-Joyner-Halenda (BJH) method. The structural properties of the samples were examined by X-ray powder diffraction (XRD) on

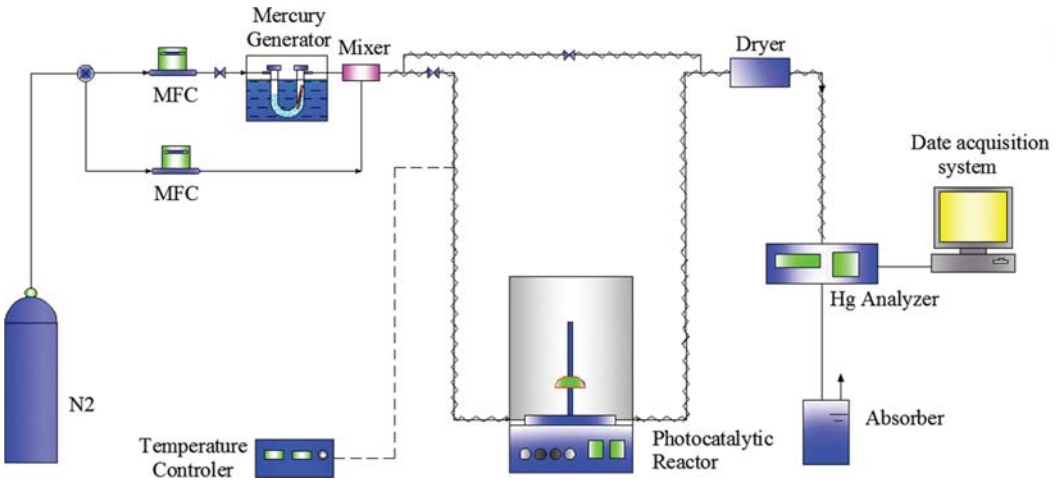

Fig. 1. Schematic diagram of the experimental system.

a BRUKER DADVANCE Diffractometer with Cu Kα radiation (λ=1.5406 Å, 40 mA and 40 kV). The scanning speed was kept at 2°/min and the scanning range covered 10-80°. Raman spectra were recorded at room temperature using a Raman spectrometer (Horiba Jobin Yvon XploRA) in the backscattering geometry with a 532 nm Ar laser as an excitation source. The UV-Vis diffuse reflectance spectra (UV-vis DRS) were recorded at room temperature in the range of 250-1,000 nm using a UV-vis spectrophotometer (SHIMADZU UV-3600 Plus, Japan) equipped with an integrating sphere, using $BaSO_4$ as the reflectance sample. The photoluminescence (PL) spectra of the materials were acquired on a fluorescence spectrophotometer (SHIMADZU RF5301, Japan) at an excitation wavelength of 360 nm. X-ray photoelectron spectroscopy (XPS) measurements were performed by Al Kα X-ray (hm=1,486.6 eV) radiation operated at 250 W (PHI5300, USA) to investigate the surface properties. The energy scale was internally calibrated by referencing the binding energy of the C1s peak at 284.6 eV for contaminated carbon.

5. Evaluation of Photocatalytic Activity

A bench-scale experimental system was assembled to evaluate catalytic activity, which was similar to that used in our previous study and was shown in Fig. 1. The system consisted of simulated flue gas generating system, photocatalytic reactor and an on-line mercury analyzer. The reactor was constructed to allow for a total N_2 flow of 1.2 L/min, at room temperatures, which was divided into two branches: one of N_2 streams with a flow rate of 1 L/min, and the other stream of N_2 with a flow rate of 0.2 L/min, passed through the Hg^0 permeation tube to introduce Hg^0 vapor to the system. One tee valve was installed on the pipeline, the main stream passed through the photocatalytic reactor, and the bypass did not pass through the photocatalytic reactor. The mercury permeation tube was placed in a U-shaped glass tube, which was immersed in a water bath at constant temperature (55 °C) to ensure a constant Hg^0 permeation rate. During the test, the mercury inlet gas bypassed the reactor until the desired inlet mercury concentration was established.

The reactor was a flat-plate photocatalytic reactor, including a square cell (90×90×10 mm) and a lid of the quartz glass (90×90 mm). LED lamp (24 W, white light LED) was installed on the top of reactor (50 mm), and a UV light (λ=365 nm) was installed on

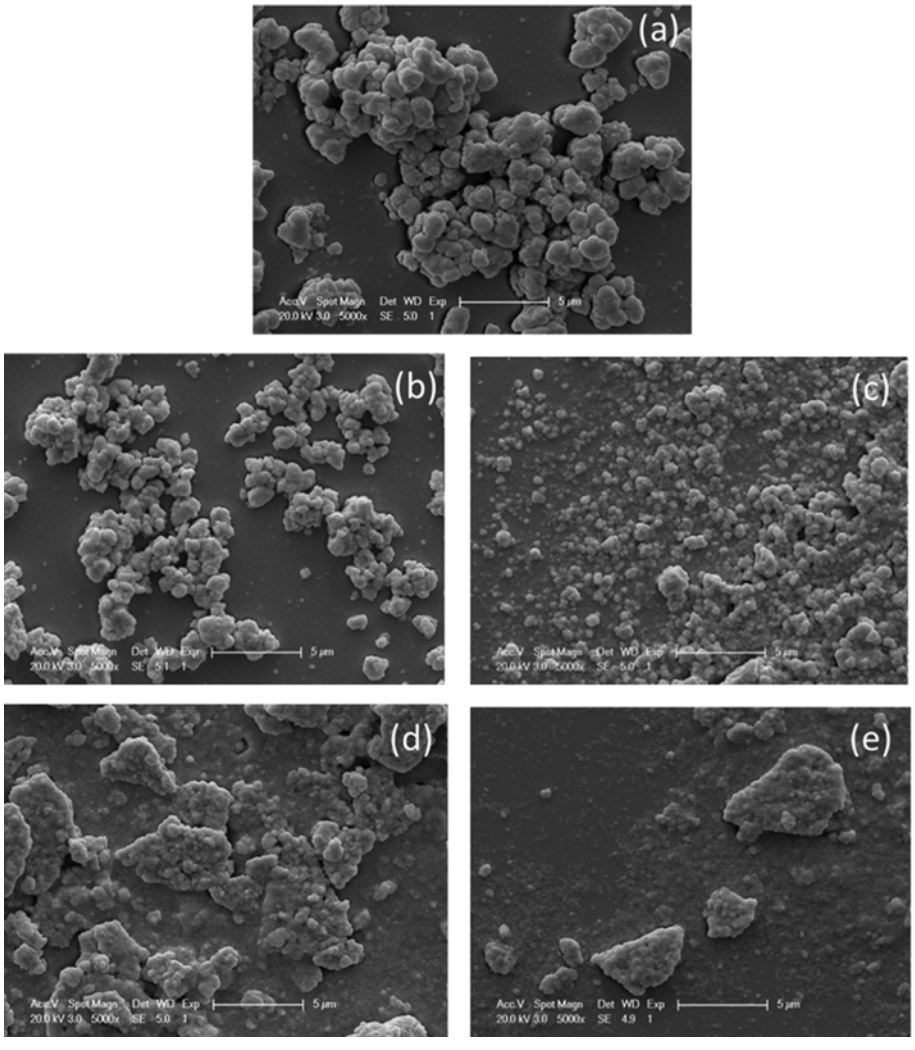

Fig. 2. Typical SEM image of TiO_2 (a), TiO_2/RGO-1 (b), TiO_2/RGO-2 (c), TiO_2/RGO-3 (d), TiO_2/RGO-4 (e).

the top of reactor (200 mm). In all experiments, the catalysts (about 50 mg) were loaded on the square glass plates (75×75 mm) by using a dip-coating method, and put into the photocatalytic reactor.

An on-line mercury analyzer (VM-3000 Mercury vapor monitor, Mercury Instruments, Germany) based on atomic absorption spectrometry was used to measure the gas phase concentration of Hg^0. The gas flowed through silica gel before entering the mercury analyzer to capture water vapor and prevent corrosion of the mercury analyzer.

The Hg^0 removal efficiency (η) was calculated according to Eq. (1).

$$\eta(\%)=\frac{Hg^0_{in}-Hg^0_{out}}{Hg^0_{in}}\times 100\% \quad (1)$$

where Hg^0_{in} and Hg^0_{out} represent the concentration of Hg^0 at the inlet and outlet of the photocatalytic reactor, respectively.

RESULTS AND DISCUSSION

1. Samples with Different Content of Graphene Oxide (GO)

The morphology of as-prepared samples with different content of GO was characterized by FESEM (Fig. 2). TiO_2 and RGO got together closely during the hydrothermal process, and the intimate interaction enables the electron to more easily transfer from TiO_2 particles to reduce GO during the photocatalytic process [31]. Particles with average diameter have a tendency to decrease, which suggested that functional groups on the surface of GO might have acted as active sites in the titanium dioxide formation process, and functional groups were the center of growth. With the increase of GO content, the increase of the content of functional groups promoted the dispersion of titanium dioxide at the interface and made the particle size of TiO_2 slightly smaller than pure TiO_2. Therefore, it could be concluded that the content of GO and its functional groups acted as a morphological controller to direct the self-organization of TiO_2 particles with different diameters. Note that RGO graphitization degree increased with the increased of the content of GO in the process of sample preparation.

As can be seen from Fig. 3(a) and (b), the RGO was retained in the form of sheets with nanometer-long wrinkles after the hydrothermal treatment of GO. Fig. 3(c) showed that TiO_2 particles were assembled with nanoparticles and the structure of surface junction at the interface of TiO_2 and RGO. The size of the TiO_2 nanocrystallites was quite uniform and was estimated to be around 10-15 nm. Moreover, the image in Fig. 3(d) indicates a well-crystallized structure with lattice spacing of 0.35 nm corresponding to the (101) planes of anatase TiO_2.

It can be seen from Fig. 4(a) that GO exhibited a characteristic peak at 2θ=ca. 10° [32,33] and the peak at 26.6° for the original

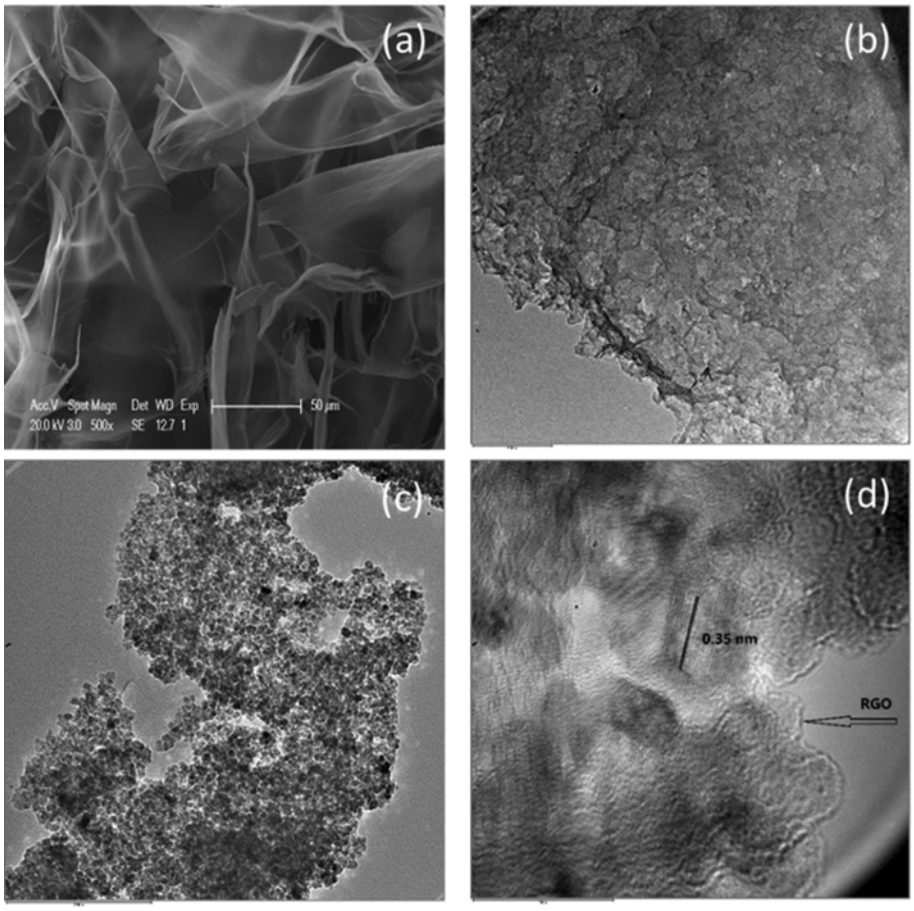

Fig. 3. SEM images of GO (a), TEM images of RGO (b) and TiO_2/RGO (c), HRTEM images of TiO_2/RGO (d).

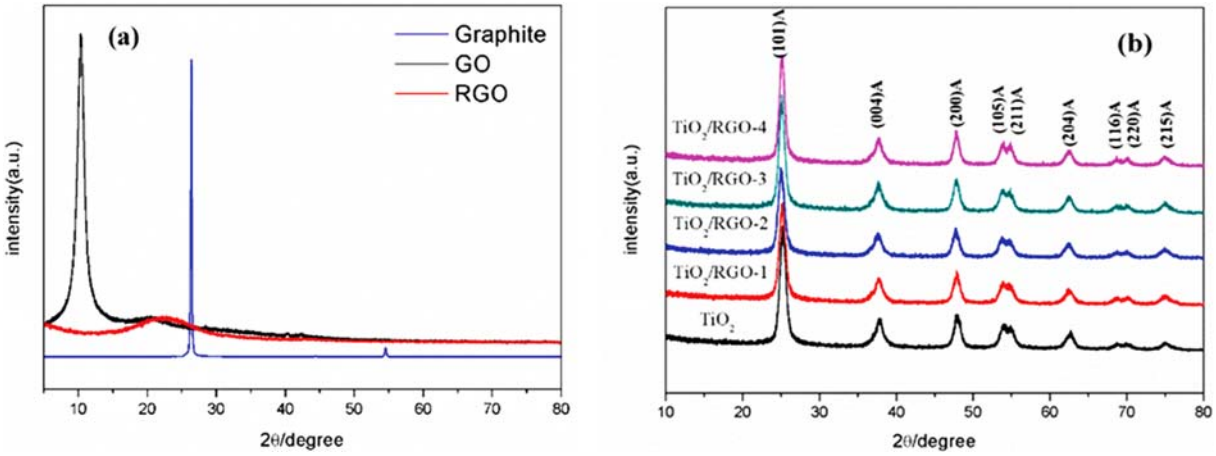

Fig. 4. XRD patterns of the Graphite, GO and RGO (a), XRD patterns of the TiO_2/RGO composites with added different content (b).

graphite. After hydrothermal reduction, a broad peak around 2θ= 22.5° appeared, which could be attributed to the corrugated RGO structure after the thermal reduction of functional groups in GO [34,35].

Fig. 4(b) shows the XRD patterns of the samples to characterize the crystalline structure. No characteristic diffraction peaks of RGO were observed in all the graphene/TiO_2 composites, which could be explained by the small amounts, high dispersion and low crystallinity of RGO [36]. Anatase phase of TiO_2 (JCPDS no. 21-1272) was observed in pure TiO_2 and TiO_2/RGO composite photocatalysts, and the characteristic diffraction peaks at 25.3°, 37.8°, 48.0°, 53.9°, 55.1°, 62.8°, 68.7°, 70.3° and 75.0° existed, which was attributed to the (101), (004), (200), (105), (211), (204), (116), (220) and (215) faces of anatase TiO_2. The average anatase crystalline grain size of the (101) peak was estimated by Scherrer's formula [15,37] and summarized in Table 1.

Table 1. Effects of GO content on the physical and chemical properties of the graphene/TiO_2 samples studied

Photocatalysts	Crystal size (nm)	Absorbing boundary (nm)	Bandgap (eV)
TiO_2	10.9	391	3.17
TiO_2/RGO-1	11.1	409	3.03
TiO_2/RGO-2	10.8	422	2.94
TiO_2/RGO-3	12.1	439	2.82
TiO_2/RGO-4	12.2	522	2.37

Fig. 5 shows the UV-visible diffuse reflectance spectroscopy of as-prepared TiO_2/RGO composite, which demonstrates that TiO_2 exhibited no absorption in the visible region of 400-800 nm, which accorded with the intrinsic absorption property of TiO_2 [38]. All the TiO_2/RGO composites extended their broad background absorption in the visible-light region, and the absorption intensity obviously increased with increasing amount of RGO in the composites. Hence, the RGO could introduce a sensitization effect to extend the response of TiO_2 into the visible-light range of the solar spectrum and be incorporated to the lattice of TiO_2 to improve absorption of photons. The optical band gap energy (E_g) of the photocatalysts was calculated based on the absorption spectrum of the samples according to equation $E_g=1240/\lambda_{Absorp.\,Edge}$ [39]. The results are shown in Table 1.

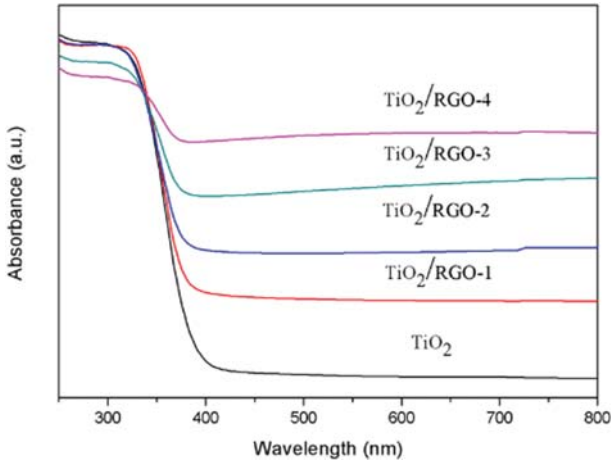

Fig. 5. UV-vis diffuse reflection spectra of TiO_2/RGO composites with added different content of GO.

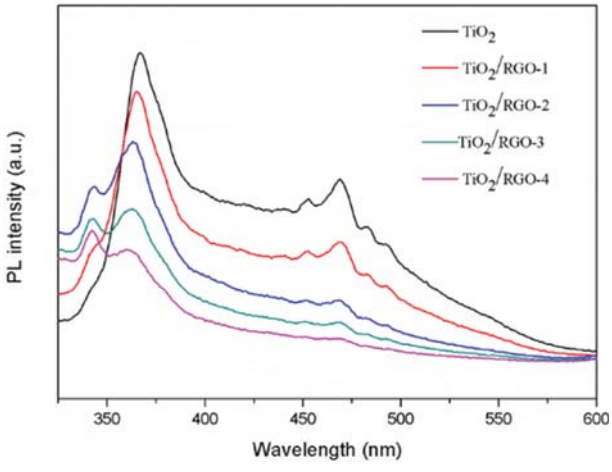

Fig. 6. Photoluminescence spectra for TiO_2/RGO composites with added different content.

Photoluminescence spectra (PL) can confirm the efficiency of charge carrier trapping and recombination in semiconductor particles by measuring the emission intensity coming from the recombination of free charge carriers [40-42]. Fig. 6 shows the PL spectra of composites recorded at room temperature, with different content of GO. PL intensity of TiO_2/RGO was much lower than that of TiO_2, which indicates that theTiO_2/RGO composites had lower recombination rate of electrons and holes under UV-light irradiation. The electrons were excited from the valence band of TiO_2 to the conduction band and then transferred to RGO due to its electronic conductivity, preventing a direct recombination of electrons and holes. The other four peaks observed in the wavelength ranging from 440 to 500 nm were attributed to excitonic PL, which mainly resulted from surface oxygen vacancies and defects [43].

2. Samples with Different Degree of Oxidation of Graphene Oxide (GO)

Raman spectroscopy was used to characterize the crystalline quality of graphene in TiO_2/RGO composites, as shown in Fig. 7. Two additional peaks at ~1,350 cm^{-1} and ~1,595 cm^{-1} were observed for composites, which could be attributed to the D and G band of carbon, respectively [44,45]. In addition, the D band was related to the presence of sp3 defects; the G band was related to the in-plane vibration of sp2 carbon atoms; and the intensity ratio of D band to G band (I_D/I_G) showed the graphitization degree of carbon [46]. For the composites TiO_2/RGO(3), TiO_2/RGO(5), TiO_2/RGO(7) and TiO_2/RGO(9), I_D/I_G are 0.75, 0.8, 0.87 and 0.94, respectively. It indicated that the defect degree of RGO in samples rose gradually, which was attributed to the extended reaction time of GO prepara-

Table 2. Effects of GO oxidation degree on the physical and chemical properties of the graphene/TiO_2 samples studied

Photocatalysts	S_{BET} (m^2/g)	Crystal size (nm)	Absorbing boundary (nm)	Bandgap (eV)
TiO_2/RGO(3)	147.6	13.7	512	2.42
TiO_2/RGO(5)	167.7	11.8	578	2.15
TiO_2/RGO(7)	148.0	11.9	625	1.98
TiO_2/RGO(9)	146.2	13.1	565	2.19

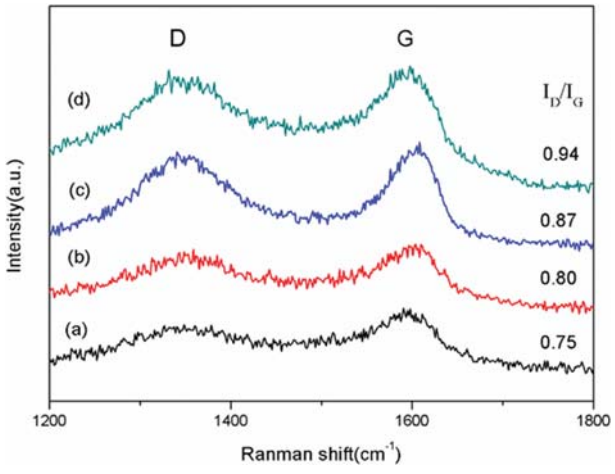

Fig. 7. Raman spectra of the samples TiO_2/RGO(3) (a), TiO_2/RGO(5) (b), TiO_2/RGO(7) (c), TiO_2/RGO(9) (d).

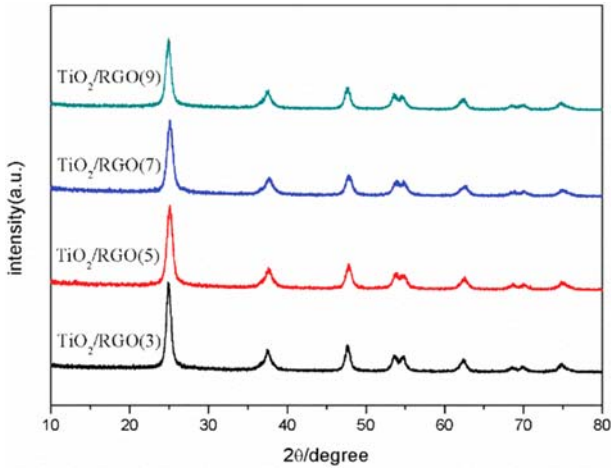

Fig. 8. XRD patterns of the TiO_2/RGO composites with added different degree of oxidation of GO.

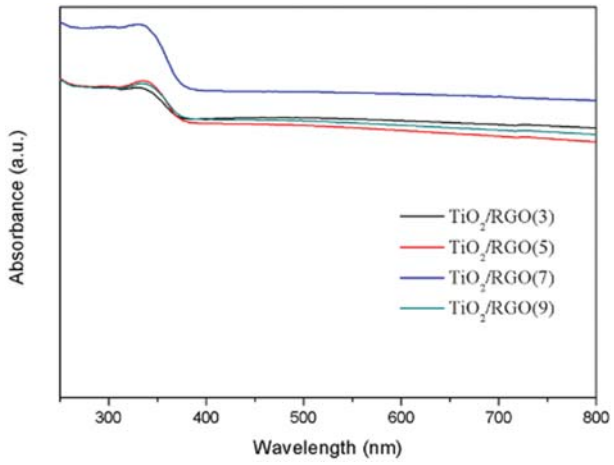

Fig. 9. UV-vis diffuse reflection spectra of TiO_2/RGO composites with added different degree of oxidation of GO.

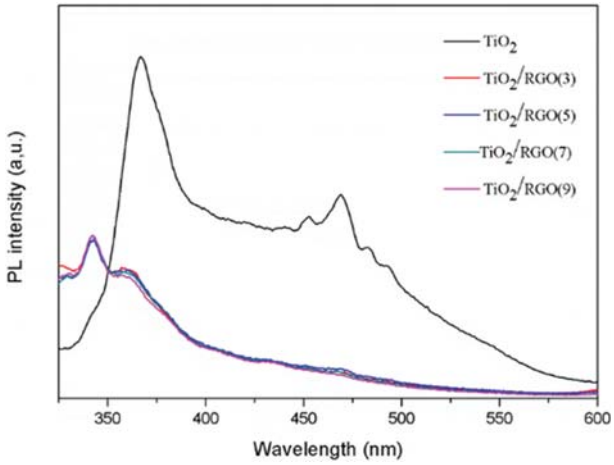

Fig. 10. Photoluminescence spectra for TiO_2/RGO composites with added different degree of oxidation of GO.

tion. With additional reaction time, the functional groups on graphite increased, improving its oxidation degree and eventually added more defects after getting rid of the functional groups by hydrothermal reaction.

It could be found from Fig. 8 that the anatase (101) diffraction peak became sharper with the decrease of degree of oxidation of GO, indicating crystallinity of the anatase phase was enhanced [47]. The average anatase crystalline grain sizes of the (101) peak is summarized in Table 2. All results indicated that different amount of GO could cause the change of the crystal sizes. By increasing the content of GO and the degree of oxidation of GO, its crystal sizes increased initially and decreased afterwards. It may safely be concluded that the content of functional groups could control the TiO_2 grain size, and the morphology of the nanocrystals formed on graphene could be tailored by the degree of oxidation of graphene. The degree of oxidation of GO could be demonstrated by Raman spectrum as shown in Fig. 7, i.e., under the same experimental conditions, high degree of oxidation of GO results in high degree of defects of RGO after hydrothermal reaction.

Fig. 9 shows the UV-vis diffuse reflection spectra of compounds, in which RGO had different defect levels. It was found that the absorbing boundary was not linearly changed with the oxidation degree of GO. The optical band gap energies (E_g) of the photocatalysts are shown in Table 2. All data obviously revealed that the ab-

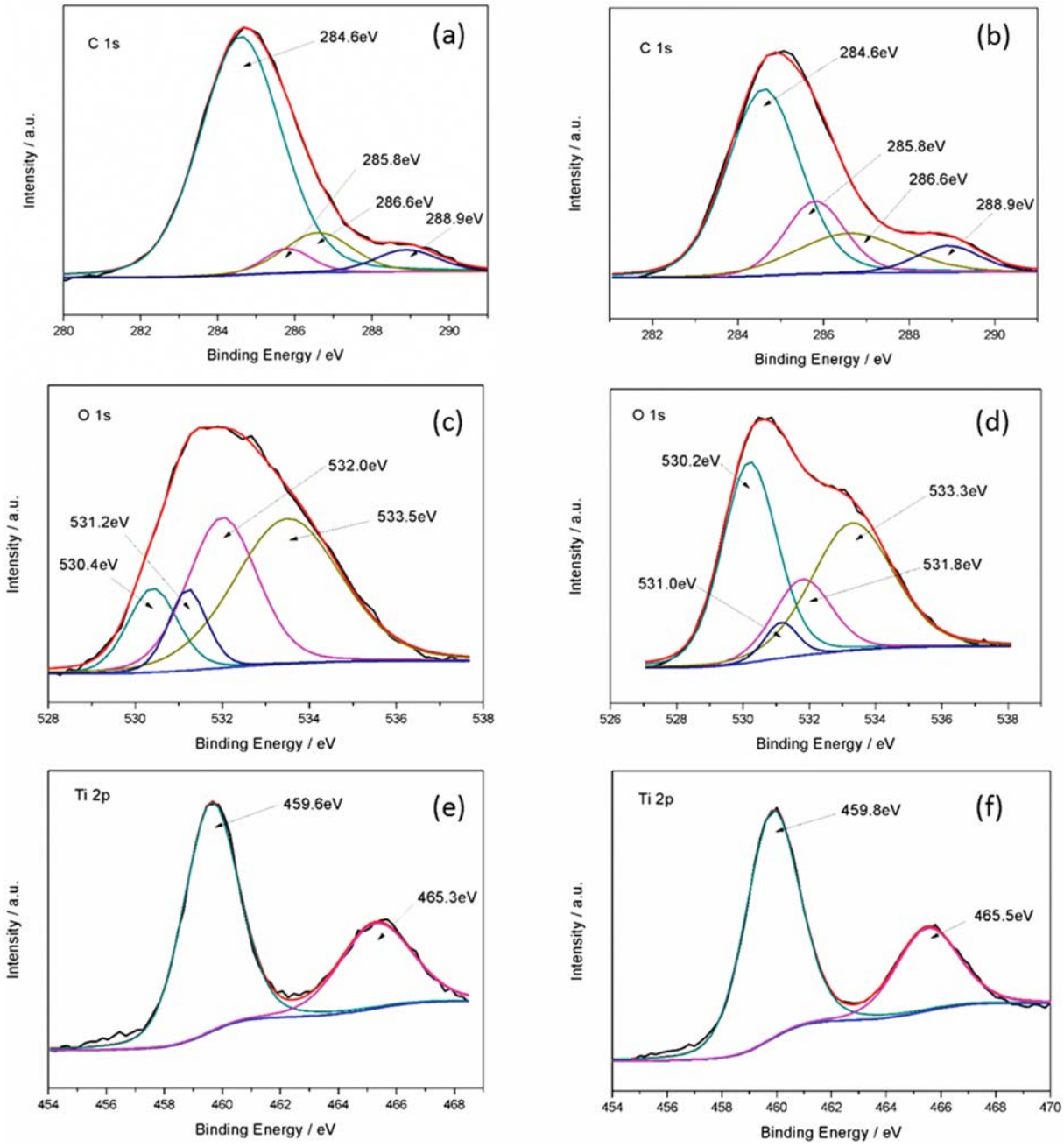

Fig. 11. XPS spectra of TiO_2/RGO, C1s ((a), (b)), O1s ((c), (d)) and Ti2p ((e), (f)) for composite before and after UV irradiation.

sorption edge of the photocatalysts progressively shifted to lower energy with increasing levels of RGO loading. Red-shift for TiO_2/RGO was also confirmed by previous investigators [48-50]. With the increase of graphene defect degree, the bandgap width of the compounds increased in first and decreased at last. The samples TiO_2/RGO(5) and TiO_2/RGO(7) showed lower bandgap, which might be the result of a good balance between the size of the crystalline grain and degree of crystallinity as shown in Fig. 4. A discussion of its effects on photocatalytic reaction is made in Table 2.

As can be seen from Fig. 10, composites with certain amount of different oxidation degree of GO were added in the process of preparation, whose recombination rates of electrons and holes of the four TiO_2/RGO samples were almost equal, while they had different degree levels of defect. It may be indicated that the efficiency of charge carrier recombination was not influenced by oxidation degree of GO or decided by the balance among conductivity of RGO, TiO_2 crystalline grain size, electron capture ability and crystallinity.

To reveal the chemical states of C, O, and Ti in the TiO_2-RGO, these samples were characterized by X-ray photoelectron spectroscopy (XPS), and the results are shown in Fig. 11, and Table 3 gives the percentages of carbon and oxygen states in these compounds. Fig. 11(a) and (b) show the C1s XPS spectra of composites before and after UV lamp irradiation, respectively. Four typical peaks of samples were located at 284.6, 285.8, 286.6, and 288.9 eV, which were usually assigned to sp2 carbon, sp3-hybridized carbon from the RGO, C-O bond [51], and carboxyl carbon (O=C-O) [31], respectively. Among them, O=C-O bonds formation mechanism was shown in Scheme 1, which indicates that the -OH groups on the TiO_2 particles possibly reacted with the -COOH groups on the GO surface through esterification to form O=C-O-Ti bonds [31].

Table 3. Percentages of different carbon and oxygen states in TiO_2/RGO before and after mercury removal under UV irradiation

	TiO_2/RGO	Before UV irradiation	After UV irradiation
Carbon states	sp2 C (%)	78	56
	sp3 C (%)	5	19
	C-O (%)	11	18
	O=C-O (%)	6	7
Oxygen states	Ti-O-Ti (%)	13	39
	C=O (%)	10	6
	Ti-OH (%)	32	17
	C-OH (%)	45	38

The absence of C 1s peak around 281 eV generally attributed to Ti-C bond excluded the possibility of carbon-doping in TiO_2 lattice [52]. After mercury removal, the relative concentration ratio of the sp2 carbon to sp3-hybridized carbon decreased from 15.6 to 2.9, indicating that the defects of RGO increased. The relative concentration of O=C-O-Ti bonds showed negligible change, which demonstrates that UV illumination did not affect the structure.

Fig. 11(c) shows that four peaks of 530.4, 531.2, 532.0, and 533.5 eV have been fitted, which was ascribed to Ti-O-Ti (lattice O), C=O (and COO), Ti-OH, and C-OH (and C-O-C) species, respectively [53-55]. And the O1s binding energies for the composites displayed a clear shift, a negative shift of 0.2 eV for the TiO_2-RGO, indicating lattice distortion arose [56] after UV irradiation. Notably, it can be found from Table 3 that the relative concentration of Ti-O-Ti/Ti-OH increased from 0.37 to 2.3, so a conclusion might be drawn that chemical bonds of Ti-OH ruptured and transformed to Ti-O-Ti under UV light.

Fig. 11(e) and (f) show XPS spectra at the Ti2p binding energy region before and after UV irradiation. The bands located at binding energies of 459.6 and 465.3 eV (459.8 and 465.5 eV after UV illumination) were assigned to the Ti(2p1/2) and Ti(2p3/2) spin-orbital splitting photoelectrons in the Ti^{4+} chemical state, respectively. The slitting between the two bands was also found at 5.7 eV. There was a positive shift of 0.2 eV for the TiO_2-RGO after UV light illumination. The higher binding energy suggested titanium changed into a relatively higher oxidation state [57,58], which might be as a result of the surface hydroxyl group of Ti-OH being transformed to Ti-O-Ti.

3. Photocatalytic Activity

To compare the photocatalytic activity of the pure TiO_2 and TiO_2/RGO composites, a series of experiments were carried out by using mercury as a model pollutant under UV and LED light irradiation with the same conditions. As can be seen from Fig. 12(a), the Hg removal efficiency under LED and UV light with the increase of content of RGO increased in first and finally decreased. The results indicate that the TiO_2/RGO composites displayed a significantly improved oxidation efficiency of mercury compared with pure TiO_2 under LED light especially the TiO_2/RGO-2 composite and the mercury removal efficiency increased more than 67%. The enhanced photocatalytic activity resulted from the good distribution of TiO_2 particles and the unique properties of graphene. Graphene acted as an electron-acceptor material to effectively hinder the electron-hole pair recombination, and a photo-sensitizer to enhance the utilization of visible light in photocatalysis [48]. However, the efficiency of TiO_2/RGO composites was lowered slightly under UV light except TiO_2/RGO-1. It was presumed the reason why efficiency

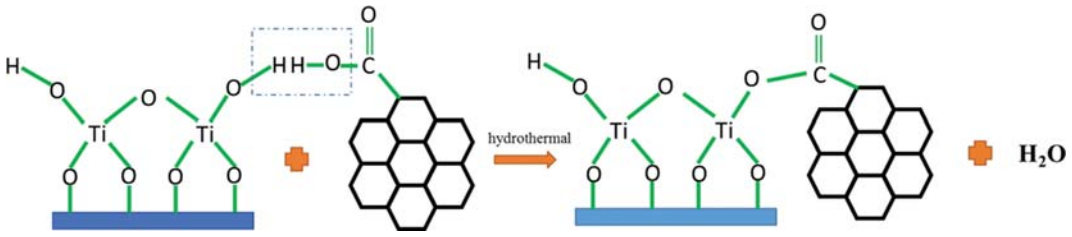

Scheme 1. The formation mechanism of O=C-O-Ti bonds.

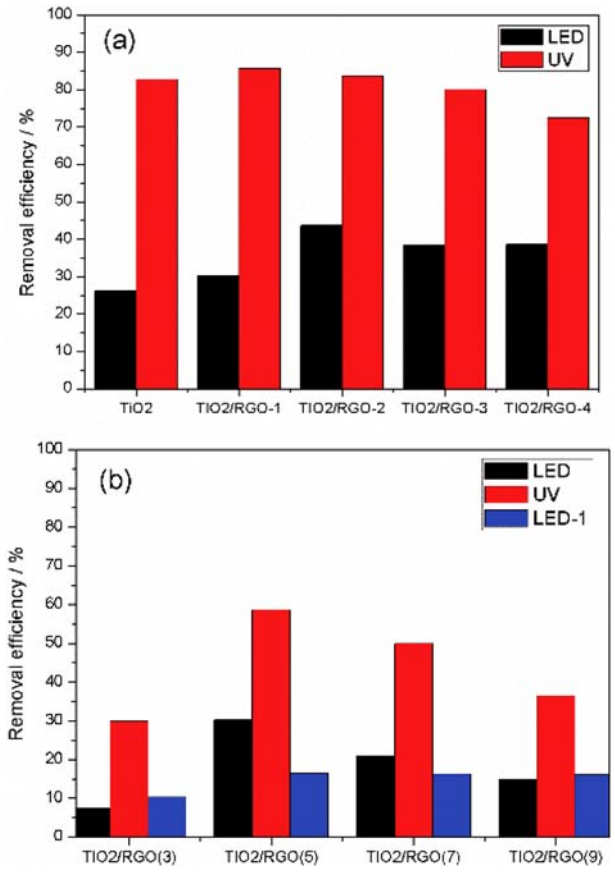

Fig. 12. The mercury removal efficiency of TiO_2-RGO with different contents of graphene (a) and different degree of oxidation of GO (b).

decreased with the increasing contents of RGO was that a high amount of graphene exhibited a strong absorption to light, thus reducing the light absorption on TiO_2 surface, resulting in the decrease of photo-excited electrons.

As shown in Fig. 12(b), the performance of photocatalyst under LED and UV light was evaluated, respectively. Titanium dioxide was modified by different oxidation degree of GO, and then LED lamp was adopted for mercury removal once again to study the change of photocatalyst properties after UV lamp irradiation (LED-1). To find the influence of different oxidation degree of GO on photocatalytic properties, different amounts of oxidation degree of GO in the process of preparation were added, which resulted in the lower efficiency of mercury removal. It can be seen that under UV and LED light with the increased of oxidation degree of GO, the Hg removal efficiency increased first and then decreased. This could be explained from Table 2, which shows the bandgap of TiO_2/RGO(5) and TiO_2/RGO(7) composites is 2.15 and 1.98 eV. However, the mercury removal efficiency of TiO_2/RGO(7) was lower than that of TiO_2/RGO(5). This might be explained that BET specific surface area of TiO_2/RGO(7) was lower than TiO_2/RGO(5), and redox level of TiO_2/RGO(7) was negative with respect to •OH/OH^- (+1.99 eV) couple, weakening the ability of oxidation capacity [30].

After UV irradiation, the mercury removal efficiency of TiO_2/RGO(3) and TiO_2/RGO(9) composites increased, but TiO_2/RGO(5) and TiO_2/RGO(7) composites decreased. It can be seen from Table 2 that crystal sizes of TiO_2/RGO(3), TiO_2/RGO(5), TiO_2/RGO(7) and TiO_2/RGO(9) were 13.7, 11.8, 11.9 and 13.1 nm, respectively. Just as shown in Fig. 13 and Table 3, the size of the crystalline grain was enhanced with the transformation of part Ti-OH bonds into Ti-O-Ti bonds after UV irradiation, which caused lattice distortion as shown in XPS spectrum of O1s. The increase of TiO_2/RGO(3) and TiO_2/RGO(9) grain size extended the time of electron hole recombination based on larger crystal. For the other two TiO_2/RGO composites, Ti-OH is more important for photocatalytic reaction than grain size due to its smaller size, and with the decrease of Ti-OH, mercury removal efficiency decreases.

4. Photocatalytic Reaction Mechanisms

Based on above results and discussion, a schematic diagram clarifying the mercury removal mechanism by the TiO_2/RGO com-

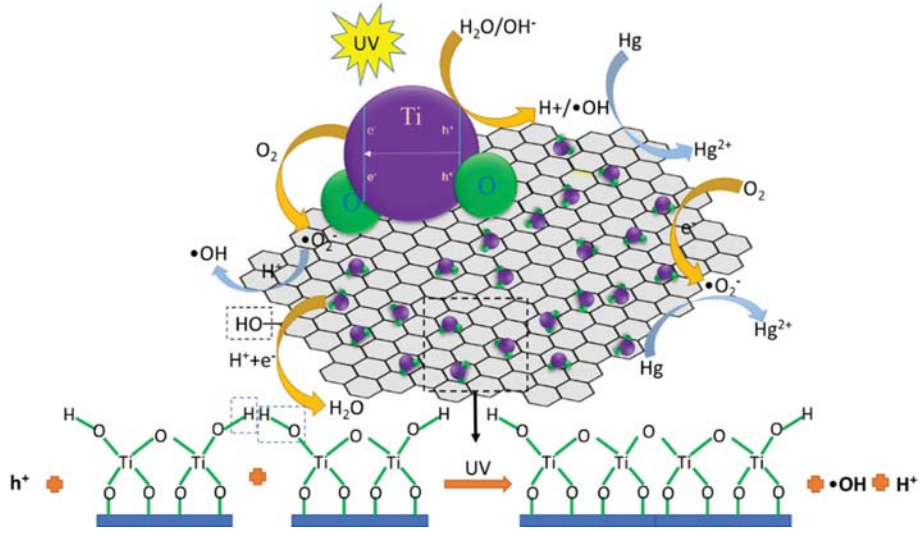

Fig. 13. Schematic illustration of mercury removal.

posite is shown in Fig. 13. The process of removing Hg can be divided into adsorption and photocatalysis: (i) Hg atoms could transfer from N_2 to the surface of TiO_2/RGO composite, (ii) The LED/UV irradiation activated TiO_2 to generate strongly oxidative holes (h^+) in valence band and reductive electrons (e^-) in the conduction band. Due to the hetero junction in the interface of RGO and TiO_2, photo-generated electrons tended to migrate from the higher Fermi level of anatase to lower Fermi level of RGO [59], which could effectively suppress photo-generated electron-hole recombination. The photo-generated holes could react with H_2O and Ti-OH to form •OH, and the photo-generated electrons may react with O_2 to form $\bullet O_2^-$, which may in turn also react with residual C-OH to form H_2O, and $\bullet O_2^-$ will react with H^+ to form •OH. It was involved the following reactions displayed in Eq. (2)-(11) [30, 60-62]. The analysis indicated that, although the nitrogen used was of ultrahigh purity (99.999%), it still contained some oxygen and water vapor.

$$TiO_2 + RGO \xrightarrow{h\nu} TiO_2(h^+) + RGO(e^-) \quad (2)$$

$$H_2O \rightleftharpoons H^+ + OH^- \quad (3)$$

$$TiO_2(h^+) + H_2O \rightarrow TiO_2 + \bullet OH + H^+ \quad (4)$$

$$RGO(e^-) + O_2 \rightarrow RGO + \bullet O_2^- \quad (5)$$

$$\bullet O_2^- + 2H^+ \rightarrow 2\bullet OH \quad (6)$$

$$OH^- + h^+ \rightarrow \bullet OH \quad (7)$$

$$Ti\text{-}OH + HO\text{-}Ti + h^+ \rightarrow Ti\text{-}O\text{-}Ti + H^+ + \bullet OH \quad (8)$$

$$RGO\text{-}OH + e^- + H^+ \rightarrow RGO + H_2O \quad (9)$$

$$Hg^+ + \bullet OH + H^+ \rightarrow Hg^{2+} + H_2O \quad (10)$$

$$2Hg^0 + \bullet O_2^- \rightarrow 2HgO \quad (11)$$

CONCLUSION

GO with different oxidation levels and enhanced photocatalytic activity was successfully synthesized by tailoring oxidation degrees and content of GO. It was found that TiO_2 crystalline grain and particle size had been tailored by the amount of functional groups, and crystallinity was also controlled by GO degrees of oxidation to enhance the photocatalytic performance under UV lamp, especially under visible light. The results showed that TiO_2/RGO photocatalysts had great efficiency in mercury removal and were impacted by crystalline grain size, surface chemical bonds and crystallinity. Moreover, the mechanism of photocatalytic reaction was explained. The present work on preparation of catalysts and pollutant treatment may be meaningful to understand the relative mechanism and improved catalytic activity.

ACKNOWLEDGEMENTS

This work was partially sponsored by National Natural Science Foundation of China (21237003, 50806041, 51106133, 51606115), Natural Science Foundation of Shanghai (18ZR1416200, 16ZR1413500).

REFERENCES

1. C. H. Lamborg, C. R. Hammerschmidt, K. L. Bowman, G. J. Swarr, K. M. Munson, D. C. Ohnemus, P. J. Lam, L.-E. Heimbürger, M. J. Rijkenberg and M. A. Saito, *Nature*, **512**, 65 (2014).
2. D. A. Cristol, R. L. Brasso, A. M. Condon, R. E. Fovargue, S. L. Friedman, K. K. Hallinger, A. P. Monroe and A. E. White, *Science*, **320**, 335 (2008).
3. J. Qiu, *Nature*, **493**, 144 (2013).
4. J. Li, N. Yan, Z. Qu, S. Qiao, S. Yang, Y. Guo, P. Liu and J. Jia, *Environ. Sci. Technol.*, **44**, 426 (2010).
5. H. Yang, Z. Xu, M. Fan, A. E. Bland and R. R. Judkins, *J. Hazard. Mater.*, **146**, 1 (2007).
6. R. Leary and A. Westwood, *Carbon*, **49**, 741 (2011).
7. A. Fujishima, K. Hashimoto and T. Watanabe, *Surf. Sci. Rep.*, **63**, 515 (2008).
8. K. Hashimoto, H. Irie and A. Fujishima, *Jpn. J. Appl. Phys.*, **44**, 8269 (2005).
9. C. Xiaobo, *Chinese J. Catal.*, **30**, 839 (2009).
10. X. Chen and S. S. Mao, *Chem. Rev.*, **107**, 2891 (2007).
11. A. Heller, *Accounts Chem. Res.*, **28**, 503 (1995).
12. Z. Zhang, C. Shao, L. Zhang, X. Li and Y. Liu, *J. Colloid Interface Sci.*, **351**, 57 (2010).
13. M.-Z. Ge, S.-H. Li, J.-Y. Huang, K.-Q. Zhang, S. S. Al-Deyab and Y.-K. Lai, *J. Mater. Chem. A*, **3**, 3491 (2015).
14. Q. Zhang, J.-B. Joo, Z. Lu, M. Dahl, D. Q. Oliveira, M. Ye and Y. Yin, *Nano Res.*, **4**, 103 (2011).
15. B. J. Ji, Q. Zhang, M. Dahl, I. Lee, J. Goebl, F. Zaera and Y. Yin, *Energy Environ. Sci.*, **5**, 6321 (2012).
16. I. Robel, B. A. Bunker and P. V. Kamat, *Adv. Mater.*, **17**, 2458 (2005).
17. A. K. Geim and K. S. Novoselov, *Nature Mater.*, **6**, 183 (2007).
18. H. Wang, J. T. Robinson, G. Diankov and H. Dai, *J. Am. Chem. Soc.*, **132**, 3270 (2010).
19. J. Zhang, Z. Zhu, Y. Tang and X. Feng, *J. Mater. Chem. A*, **1**, 3752 (2013).
20. K. Woan, G. Pyrgiotakis and W. Sigmund, *Adv. Mater.*, **21**, 2233 (2009).
21. H. Zhang, X. Lv, Y. Li, Y. Wang and J. Li, *ACS Nano*, **22**, 380 (2009).
22. C. H. Kim, B.-H. Kim and K. S. Yang, *Carbon*, **50**, 2472 (2012).
23. B. C. Brodie, Philos. T. R. *Soc. B*, **149**, 249 (1859).
24. L. Staudenmaier, *Chem. Ges.*, **31**, 1481 (1898).
25. W. S. Hummers Jr. and R. E. Offeman, *J. Am. Chem. Soc.*, **80**, 1339 (1958).
26. C. Chen, W. Cai, M. Long, B. Zhou, Y. Wu, D. Wu and Y. Feng, *ACS Nano*, **4**, 6425 (2010).
27. G. Jiang, Z. Lin, C. Chen, L. Zhu, Q. Chang, N. Wang, W. Wei and H. Tang, *Carbon*, **49**, 2693 (2011).
28. C. Bao, L. Song, W. Xing, B. Yuan, C. A. Wilkie, J. Huang, Y. Guo and Y. Hu, *J. Mater. Chem.*, **22**, 6088 (2012).
29. D. C. Marcano, D. V. Kosynkin, J. M. Berlin, A. Sinitskii, Z. Sun, A. Slesarev, L. B. Alemany, W. Lu and J. M. Tour, *ACS Nano*, **4**, 4806 (2010).
30. J. Wu, C. Li, X. Zhao, Q. Wu, X. Qi, X. Chen, T. Hu and Y. Cao, *Appl. Catal. B: Environ.*, **176**, 559 (2015).
31. Q. Xiang, J. Yu and M. Jaroniec, *Nanoscale*, **3**, 3670 (2011).
32. A. J. Patil, J. L. Vickery, T. B. Scott and S. Mann, *Adv. Mater.*, **21**,

3159 (2009).
33. S. Zhang, H. Song, P. Guo, J. Zhou and X. Chen, *Carbon*, **48**, 4211 (2010).
34. S. J. An, Y. Zhu, S. H. Lee, M. D. Stoller, T. Emilsson, S. Park, A. Velamakanni, J. An and R. S. Ruoff, *J. Phys. Chem. Lett.*, **1**, 1259 (2010).
35. S. Lee, S. H. Eom, J. S. Chung and S. H. Hur, *Chem. Eng. J.*, **233**, 297 (2013).
36. X. Yu, J. Liu, Y. Yu, S. Zuo and B. Li, *Carbon*, **68**, 718 (2014).
37. J. Zhong, F. Chen and J. Zhang, *J. Phys. Chem. C*, **114**, 933 (2009).
38. W. Ren, Z. Ai, F. Jia, L. Zhang, X. Fan and Z. Zou, *Appl. Catal. B: Environ.*, **69**, 138 (2007).
39. S. Hu, F. Zhou, L. Wang and J. Zhang, *Catal. Commun.*, **12**, 794 (2011).
40. J. Yu, J. Fan and B. Cheng, *J. Power Sources*, **196**, 7891 (2011).
41. J. Yu, T. Ma, G. Liu and B. Cheng, *Dalton T.*, **40**, 6635 (2011).
42. J. Yu, T. Ma and S. Liu, *Chem. Phys.*, **13**, 3491 (2011).
43. Q. Xiang, J. Yu and M. Jaroniec, *J. Phys. Chem. C*, **115**, 7355 (2011).
44. W. Fan, Q. Lai, Q. Zhang and Y. Wang, *J. Phys. Chem. C*, **115**, 10694 (2011).
45. L. C. Sim, K. H. Leong, S. Ibrahim and P. Saravanan, *J. Mater. Chem. A*, **2**, 5315 (2014).
46. Y. Gao, X. Pu, D. Zhang, G. Ding, X. Shao and J. Ma, *Carbon*, **50**, 4093 (2012).
47. J. Lin, X. Liu, S. Zhu, Y. Liu and X. Chen, *Nano Scale Res. Lett.*, **10**, 1 (2015).
48. K. Zhou, Y. Zhu, X. Yang, X. Jiang and C. L. *New J. Chem.*, **35**, 353 (2011).
49. D. Liang, C. Cui, H. Hu, Y. Wang, S. Xu, B. Ying, P. Li, B. Lu and H. Shen, *J. Alloys Compd.*, **582**, 236 (2014).
50. C. Hou, *J. Hazard. Mater.*, **205**, 229 (2012).
51. B. Li, Z. Zhao, F. Gao, X. Wang and J. Qiu, *Appl. Catal. B: Environ.*, **147**, 958 (2014).
52. H. Irie, Y. Watanabe and K. Hashimoto, *Chem. Lett.*, **32**, 772 (2003).
53. G. An, W. Ma, Z. Sun, Z. Liu, B. Han, S. Miao, Z. Miao and K. Ding, *Carbon*, **45**, 1795 (2007).
54. N. P. Zschoerper, V. Katzenmaier, U. Vohrer, M. Haupt, C. Oehr and T. Hirth. *Carbon*, **47**, 2174 (2009).
55. J. Zhong, F. Chen and J. Zhang, *J Phys. Chem. C*, **114**, 933 (2009).
56. E. M. Neville, M. J. Mattle, D. Loughrey, B. Rajesh, M. Rahman, J. M. D. Macelroy, J. A. Sullivan and K. R. Thampi, *J. Phys. Chem. C*, **116**, 16511 (2012).
57. D.-e. Gu, Y. Lu and B.-c. Yang, *Chem. Commun.*, **21**, 2453 (2008).
58. H. Li, D. Wang, H. Fan, P. Wang, T. Jiang and T. Xie, *J. Colloid Interface Sci.*, **354**, 175 (2011).
59. D. Zhao, G. Sheng, C. Chen and X. Wang, *Appl. Catal. B: Environ.*, **111**, 303 (2012).
60. Q. Zhou, Y.-H. Zhong, X. Chen, J.-H. Liu, X.-J. Huang and Y.-C. Wu, *J. Mater. Sci.*, **49**, 1066 (2014).
61. J. Wu, K. Xu, Q. Z. Liu, Z. Ji, C. H. Qu, X. M. Qi, H. Zhang, Y. Guan, P. He and L. J. Zhu, *Appl. Catal. B: Environ.*, **232**, 135 (2018).
62. X. Zhou, J. Wu, Q. F. Li, T. Zeng, Z. Ji, P. He, W. G. Pan, X. M. Qi, C. Y. Wang and P. K. Liang, *J. Catal.*, **355**, 26 (2017).